Journal of Materials Chemistry A

ROYAL SOCIETY OF CHEMISTRY

PAPER

View Article Online
View Journal | View Issue

Cite this: J. Mater. Chem. A, 2026, 14, 15008

Central aromatic ring substitution on non-fullerene acceptors boosts the performance of organic photovoltaics

Ruibin Bian,[a] Xiangjian Cao,[a] Zhaoyang Yao,[*a] Wenkai Zhao,[b] Shuhui Ding,[a] Guankui Long,[b] Xiangjian Wan,[*a] Chenxi Li[a] and Yongsheng Chen[*a]

Molecular packings of non-fullerene acceptors (NFAs), which are determined by not only end groups but also central cores, affect the power conversion efficiency (PCE) of organic solar cells (OSCs) greatly. Compared to typical halogen and alkyl substitutions, aromatic moieties are usually more powerful in tuning molecular packing due to their π–π stacking ability. Herein, two NFAs, CH-Ph and CH-Th, were designed and synthesized with phenyl and thiophene substitutions on the central phenazine cores, respectively. A systematic investigation reveals that different aromatic substitutions on the central core result in diverse molecular planarity and frontier orbital distributions, which greatly influence the crystallinity of NFAs and their photo-dynamics in blend films. Benefiting from the enhanced crystallinity, the PM6:CH-Th-based binary organic solar cells achieved a high PCE of 18.96%, outperforming the PM6:CH-Ph-based devices (PCE = 17.89%). By incorporating CH-Th as a third component, the ternary OSCs of PM6:CH6F:CH-Th further attained an excellent PCE of 19.94%. Our findings emphasize the crucial role of aromatic substituents on the central core in tuning the crystallinity of non-fullerene acceptors and enhancing the PCE of organic solar cells.

Received 24th December 2025
Accepted 15th February 2026

DOI: 10.1039/d5ta10460b

rsc.li/materials-a

Introduction

Organic solar cells (OSCs) have attracted considerable research interest due to their inherent mechanical flexibility,[1–5] low cost,[6–10] semi-transparency,[11–16] and solution processability.[17–20] The rapid development of non-fullerene acceptors (NFAs) has propelled the power conversion efficiency (PCE) of single-junction OSCs beyond 20%.[21–28] The significant enhancement in both the short-circuit current (J_{SC}) and open-circuit voltage (V_{OC}) of the OSCs can be accounted for by the distinct advantages of A–D–A-type NFAs: their strong light-harvesting capability and their readily tunable energy levels, respectively.[29] Among them, ITIC analogs[30–33] were one of the most successful categories of NFAs, in which the end groups (E) determine molecular packings. In contrast, the superstar Y-series NFAs exhibit a three-dimensional (3D) packing arrangement, with both central unit (C) and end groups participating in intermolecular stackings.[34–36] This 3D molecular packing in Y-series NFAs has been proven to enhance charge transfer and transport dynamics, thereby improving the PCE of the corresponding devices.[37–40] With the advent of NFAs with two-dimensionally extended central units, the central units have exhibited great merits in enhancing the strength of molecular packing and optimizing the 3D packing networks. For example, a series of two-dimensional acceptors were developed by our group, and the conjugation extension of the central unit has successfully modulated molecular packing into a mode more favorable for electron transfer.[41–43] Then, Wei's group synthesized two acceptors Qx-1 and Qx-2 with aromatic modifications on the central core and the PM6:Qx-2 based devices achieved a favorable PCE of 18.2%.[44] Recently, Luo's group introduced naphthalene into the central core innovatively and synthesized three acceptors NaO1, NaO2 and NaO3. Among them, the PM6:NaO1 based devices reached an excellent PCE of 19.11%.[45] Moreover, two-dimensionally extended central units also offer extra chemical active positions for further structural modifications. Therefore, the molecular stacking of NFAs and further the phase separation features of active layers could be optimized conveniently by designing new central cores of NFAs.[46]

Several types of moieties have been employed to modify the central core, including halogens,[47,48] alkyl and alkoxyl groups,[49–51] trifluoromethyl groups,[52,53] and so on (Fig. 1a). These groups greatly impact the energy levels, absorption spectra, intermolecular interactions, and crystallinity of NFAs.[32] Compared to other functional groups, the unique feature of

[a]State Key Laboratory and Institute of Elemento-Organic Chemistry, The Centre of Nanoscale Science and Technology and Key Laboratory of Functional Polymer Materials, Renewable Energy Conversion and Storage Center (RECAST), Frontiers Science Center for New Organic Matter, College of Chemistry, Nankai University, Tianjin, 300071, China. E-mail: yschen99@nankai.edu.cn; xjwan@nankai.edu.cn; zyao@nankai.edu.cn

[b]School of Materials Science and Engineering, National Institute for Advanced Materials, Renewable Energy Conversion and Storage Center (RECAST), Nankai University, Tianjin, 300350, China

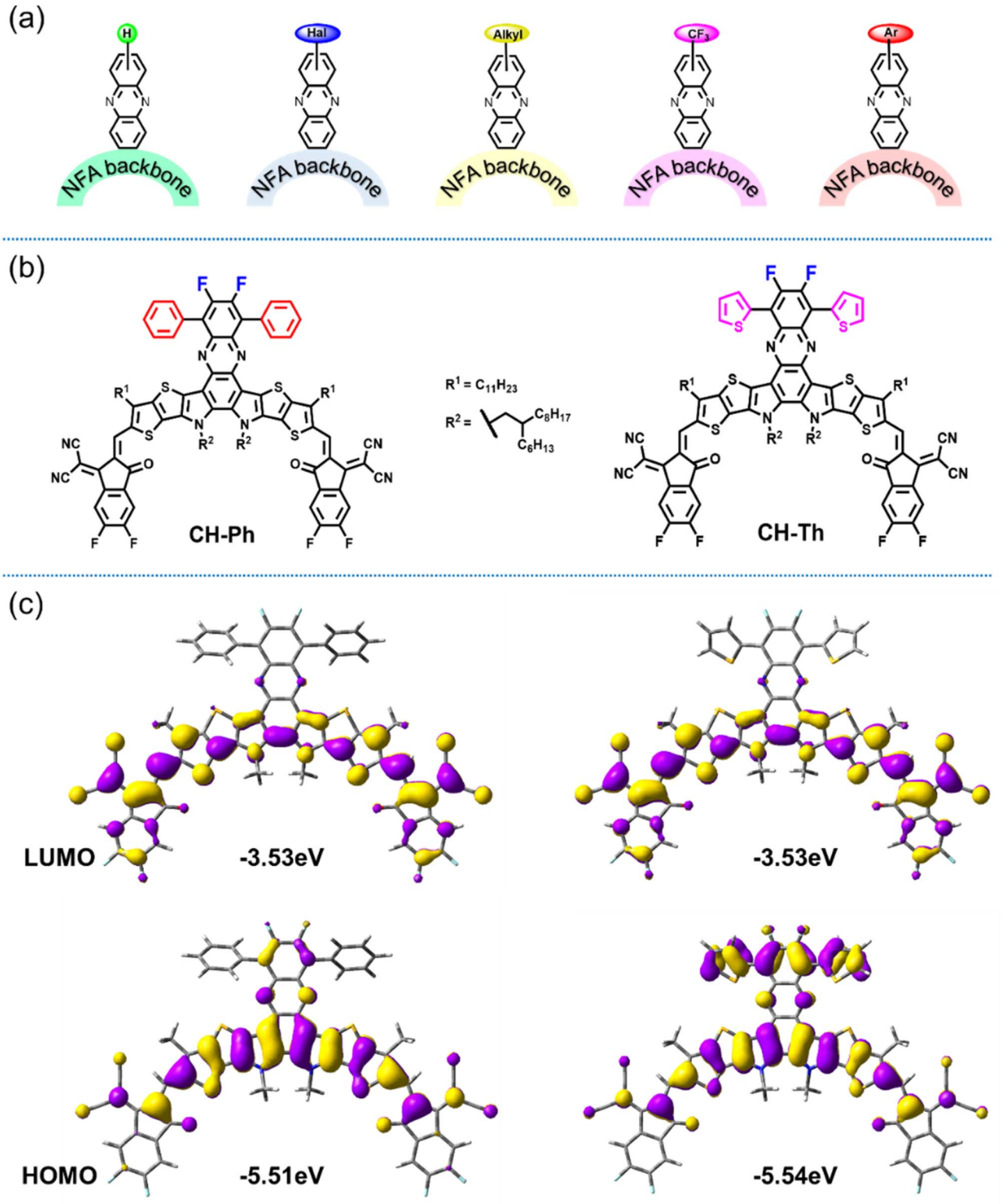

Fig. 1 (a) Various substituents on the central phenazine core of NFAs. (b) Chemical structures of CH-Th and CH-Ph. (c) Molecular frontier orbital distributions with energy levels.

aromatic moieties is the planar conjugated backbone with π–π stacking ability,[54–56] which may exert more effects on molecular packing behaviors of NFAs and miscibility between donor and acceptor materials.[57] Herein we designed and synthesized two NFAs, CH-Ph and CH-Th (Fig. 1b), based on a high-performance molecular platform of CH6F (Fig. S1),[47] with phenyl and thiophene substitutions on central phenazine cores, respectively. The quite different electrostatic and geometric features of

benzene and thiophene result in diverse molecular planarity and frontier orbital distributions. In particular, the noncovalent bonds between S-atoms on thiophenes and N-atoms on phenazine units help to maintain the planarity of CH-Th to some extent,[41] which improves the crystallinity of CH-Th and its photo-dynamics in blend films significantly. Consequently, PM6:CH-Th-based binary devices achieved a good PCE of 18.96%, surpassing the 17.89% for PM6:CH-Ph. By incorporating CH-Th as a third component, the ternary device PM6:CH6F:CH-Th attained an excellent PCE of 19.94%. Our findings highlight the effectiveness of the central aromatic substituent in adjusting the crystallinity of NFAs and, further, the PCE of OSCs.

Results and discussion

The synthesis of CH-Th and CH-Ph is outlined in Scheme S1, with detailed experimental procedures described in the Synthesis section (SI). Density functional theory (DFT) calculations (B3LYP functional[58] with 6-31G(d) basis set[59]) were performed to investigate the impact of substituted aromatic rings on the phenazine core. Both CH-Ph and CH-Th exhibit a relatively planar backbone and a typical A–D–A type structure, as indicated by the apparent peak–valley–peak property of frontier orbital charge density differences and an electrostatic surface potential analysis (Fig. S2). As thiophene is substituted on the D part of the molecule and owing to the electron-donating property of the thiophene ring, CH-Th exhibits a more pronounced A–D–A feature (Fig. S3). An enhanced A–D–A feature may enable NFAs to have a superior molecular stacking, better charge separation and transport, and smaller energy loss in the resulting OSCs.[60–63] Besides, Ch-Th presents a slightly larger polarizability than CH-Ph, which is also beneficial for enhancing dielectric properties and improving exciton dissociations (Table S1).[64–66] CH-Ph is less planar than CH-Th with a dihedral angle of 53.6° between substituted aromatic rings and phenazine core, much larger than that of CH-Th (33.2°). This could be induced by the strong noncovalent S–N secondary interactions between S-atoms on the substituted thiophene ring and N-atoms on the phenazine unit (Fig. S4). The distribution of frontier molecular orbitals of CH-Ph and CH-Th is quite different, as CH-Th has a more rigid and planar backbone. The highest occupied molecular orbital (HOMO) of CH-Th spreads to the substituted thiophene on the phenazine unit, while the corresponding phenyl rings contribute little to the HOMO of CH-Ph (Fig. 1c). The different distribution of the HOMO orbitals of CH-Th and CH-Ph results in a slightly down-shifted HOMO energy level of −5.54 eV for CH-Th compared to that of −5.51 eV for CH-Ph. Despite the diverse distribution of the HOMO, the distribution of the lowest unoccupied molecular orbital (LUMO) remains unchanged, resulting in nearly the same LUMO energy level. This resulted in a slightly larger bandgap for CH-Th than CH-Ph, which should account for the blue-shifted absorption of CH-Th in dilute chloroform solutions (Fig. 2a).

Cyclic voltammetry (CV) was performed to evaluate the energy levels of CH-Ph and CH-Th (Fig. S5). The HOMO/LUMO energy levels are estimated as −5.60/−3.90 eV for CH-Ph and −5.68/−3.87 eV for CH-Th (Fig. 2b). The derived bandgap of CH-

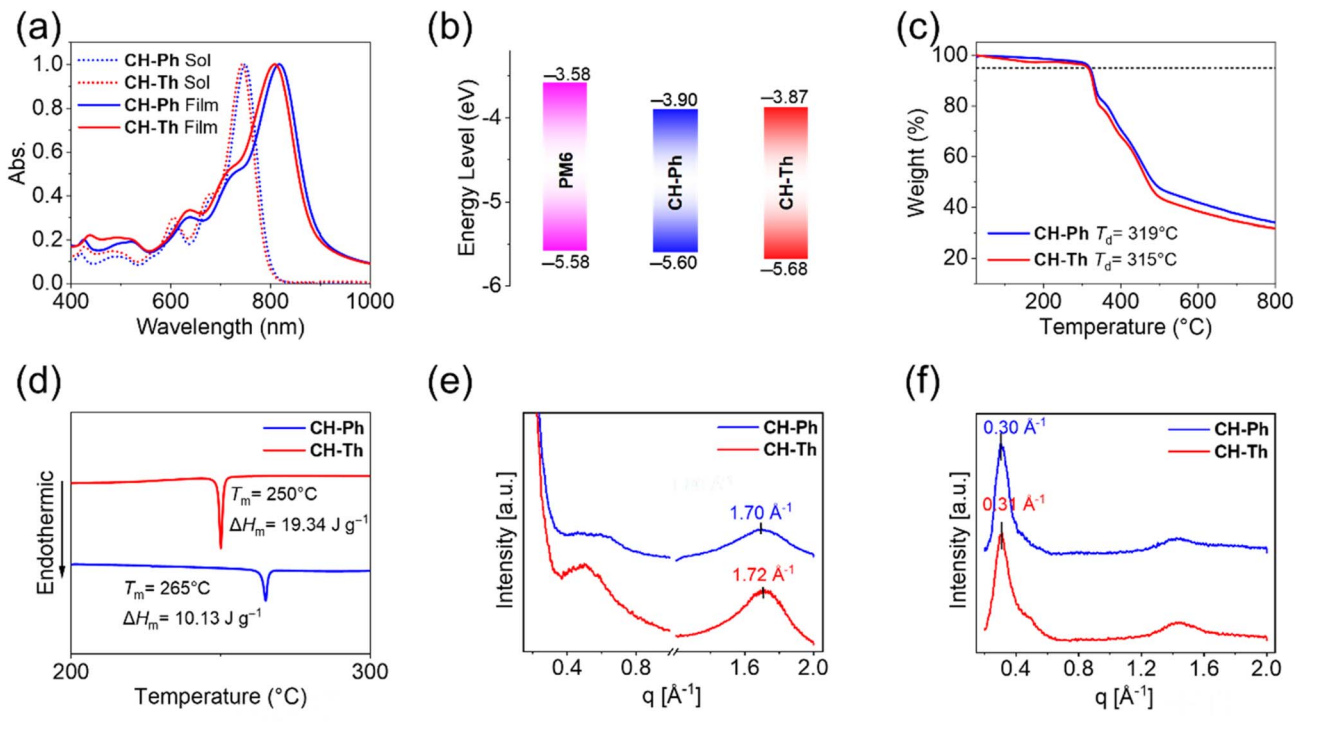

Fig. 2 (a) The absorptions of CH-Ph and CH-Th in dilute chloroform solutions and neat films. (b) The energy levels evaluated by cyclic voltammetry (CV). (c) TGA curves of CH-Ph and CH-Th. (d) DSC curves of CH-Ph and CH-Th. (e) and (f) Out-of-plane (OOP) and in-plane (IP) line cuts derived from 2D-GIWAXS of neat films.

Ph is 1.70 eV, which is smaller than that of CH-Th (1.81 eV). Therefore, the absorption of CH-Ph films is red-shifted with the maximum peak at 818 nm, followed by CH-Th at 809 nm. Due to the extended conjugated backbones enabled by the central aromatic rings, larger molar extinction coefficients of 2.62×10^5 M^{-1} cm^{-1} for CH-Th and 2.63×10^5 M^{-1} cm^{-1} for CH-Ph were observed, with respect to that of 2.10×10^5 M^{-1} cm^{-1} for CH6F (Fig. S6). Both CH-Ph and CH-Th exhibit excellent thermal stability, with decomposition temperatures exceeding 310 °C (Fig. 2c). Differential scanning calorimetry (DSC) curves (Fig. 2d) reveal exothermic peaks at 265 °C for CH-Ph and 250 °C for CH-Th, with corresponding melting enthalpies (ΔH_m) of 10.13 and 19.34 J g^{-1}, respectively. The higher melting enthalpy of CH-Th suggests stronger crystallinity compared to CH-Ph.[67] As illustrated in Fig. S7, CH-Th has a smaller exciton binding energy (E_b) of 72.2 meV than CH-Ph (93.5 meV). In theory, a smaller binding energy enables the dissociation of photogenerated excitons in CH-Th into free charges with a lower driving force, thereby further reducing the energy loss in OSCs.[68,69] We used grazing-incidence wide-angle X-ray scattering (GIWAXS) on neat films of the acceptors to investigate their molecular packing (Fig. S8). As shown in Fig. 2e and f, both acceptors exhibited a strong (010) diffraction peak in the OOP direction and a distinct (100) diffraction peak in the IP direction, consistent with a preferential face-on molecular orientation. In the OOP direction, CH-Th showed a π–π stacking distance of 3.65 Å, smaller than that of 3.69 Å for CH-Ph (Table S2). Moreover, CH-Th also displayed a notably larger crystal coherence length (CCL) of 23.77 Å compared with 16.30 Å for CH-Ph, indicating that CH-Th possesses better molecular crystallinity.

Single crystals were employed to elucidate the influence of substituted aromatic rings on molecular packing. As shown in Fig. S9 and Table S3, both acceptors adopt a C-shaped conformation with planar backbones. The dihedral angles between the two terminal planes are 10.0° for CH-Ph and 7.5° for CH-Th. Furthermore, the dihedral angles between the aromatic side groups and the central phenazine core are 45.9° for CH-Ph and 37.6° for CH-Th, indicating that CH-Th possesses a more planar backbone—a finding consistent with earlier DFT calculations. The enhanced planarity of CH-Th promotes molecular packing and crystallinity, as confirmed by GIWAXS analysis of neat films. The planarity and rigidity of CH-Th can be attributed to an intramolecular S–N interaction between the sulfur atom of the substituted thiophene ring and a nitrogen atom of the pyrazine core. The measured S–N distance derived from the single crystal is approximately 3.10 Å, which is significantly shorter than the non-bonding distance (≈3.50 Å), supporting the existence of noncovalent interactions (Fig. S9).[41] In contrast, CH-Ph lacks such a strong non-covalent interaction between its phenyl substituent and the phenazine core. CH-Th and CH-Ph exhibit rectangular-shaped voids with dimensions of ≈34.4 × 8.3 Å and 31.4 × 14.4 Å, respectively (Fig. 3a). The size and planarity of these aromatic substituents on the phenazine moiety give rise to distinct crystalline architecture and three-dimensional stacking networks, which may further affect charge separation and transport properties in photovoltaic devices.

The variation in stacking networks arises from differences in intermolecular packing modes. To analyze this, key packing modes with intermolecular interaction energies exceeding 80 kJ mol^{-1} were identified (Fig. 3b). Moreover, the single crystal of CH6F without central aromatic substitutions was also obtained from the literature in order to make a clear comparison (Fig. S10). Molecular packing usually involves three moieties: the ending group (E, red), central unit (C, blue), and bridge unit (B, yellow). Unlike CH6F, where the strongest interaction corresponds to the E/E + C/C packing mode, both CH-Th and CH-Ph exhibit a dual E/C packing mode as the dominant interaction, with energies of −448.7 kJ mol^{-1} and −460.3 kJ mol^{-1}, respectively (Fig. 3c), which is significantly higher than that of CH6F (−236.5 kJ mol^{-1}). A common trend is that substitution on the phenazine core substantially increases intermolecular interaction energies and shifts the dominant packing mode from E/E + C/C to dual E/C.[41] This highlights that both the end and central groups play key roles in driving molecular assembly. The extended conjugation in the central unit enhances π–π interactions between molecules, leading to the emergence of the E/C packing mode. The π–π stacking distances for the strongest packing modes are 3.46 Å (CH-Th), 3.55 Å (CH-Ph), and 3.57 Å (CH6F). CH-Th shows a notably shorter π–π stacking distance, which promotes tighter molecular packing—a feature beneficial for charge separation and transport.[47,70] As summarized in Table S4, the dual E/B packing mode yields the highest electron transfer integrals: 25.7 meV for CH-Ph and 12.8 meV for CH-Th. Other packing modes contribute little to electron transfer in CH-Ph, whereas in CH-Th, the C/C + E/E mode also provides another electron-transfer pathway, with an integral of 9.4 meV.

To investigate the impact of different aromatic substituents on photovoltaic performance, OSCs with conventional architecture were fabricated. Regarding the active layers, PM6 (ref. 71) was chosen as the donor for its matched energy levels and complementary absorption spectra with acceptors. The detailed device parameters are provided in the SI (Tables S5 and S6). The device based on PM6:CH-Ph achieved a better PCE of 17.89%, with a higher V_{OC} of 0.914 V, a J_{SC} of 25.30 mA cm^{-2}, and an FF of 77.36%, compared to CH6F[47] (Table S7). Notably, the PM6:CH-Th based OSC rendered a further improved PCE of 18.96%, with a V_{OC} of 0.932 V, a J_{SC} of 26.41 mA cm^{-2}, and an FF of 77.01% (Fig. 4a and Table 1). Although CH-Th has a similar bandgap with CH-Ph, CH-Th based devices exhibited higher V_{OC}s than CH-Th based devices, suggesting a lower energy loss and suppressed charge combination. Notably, CH-Th-based devices also presented better EQEs than CH-Ph (Fig. 4b), indicating better charge transfer/transportation dynamics, which results from a more planar backbone and stronger crystallinity of CH-Th. To achieve a higher PCE, CH6F was selected for fabricating ternary devices due to its red-shifted absorption in neat films and excellent miscibility with CH-Th (Fig. S11 and Table S8). As expected, the PM6:CH6F:CH-Th-based device achieved a champion PCE of 19.94% with a V_{OC} of 0.876 V, a J_{SC} of 28.24 mA cm^{-2} and an FF of 80.62% (Table 1 and S9). The

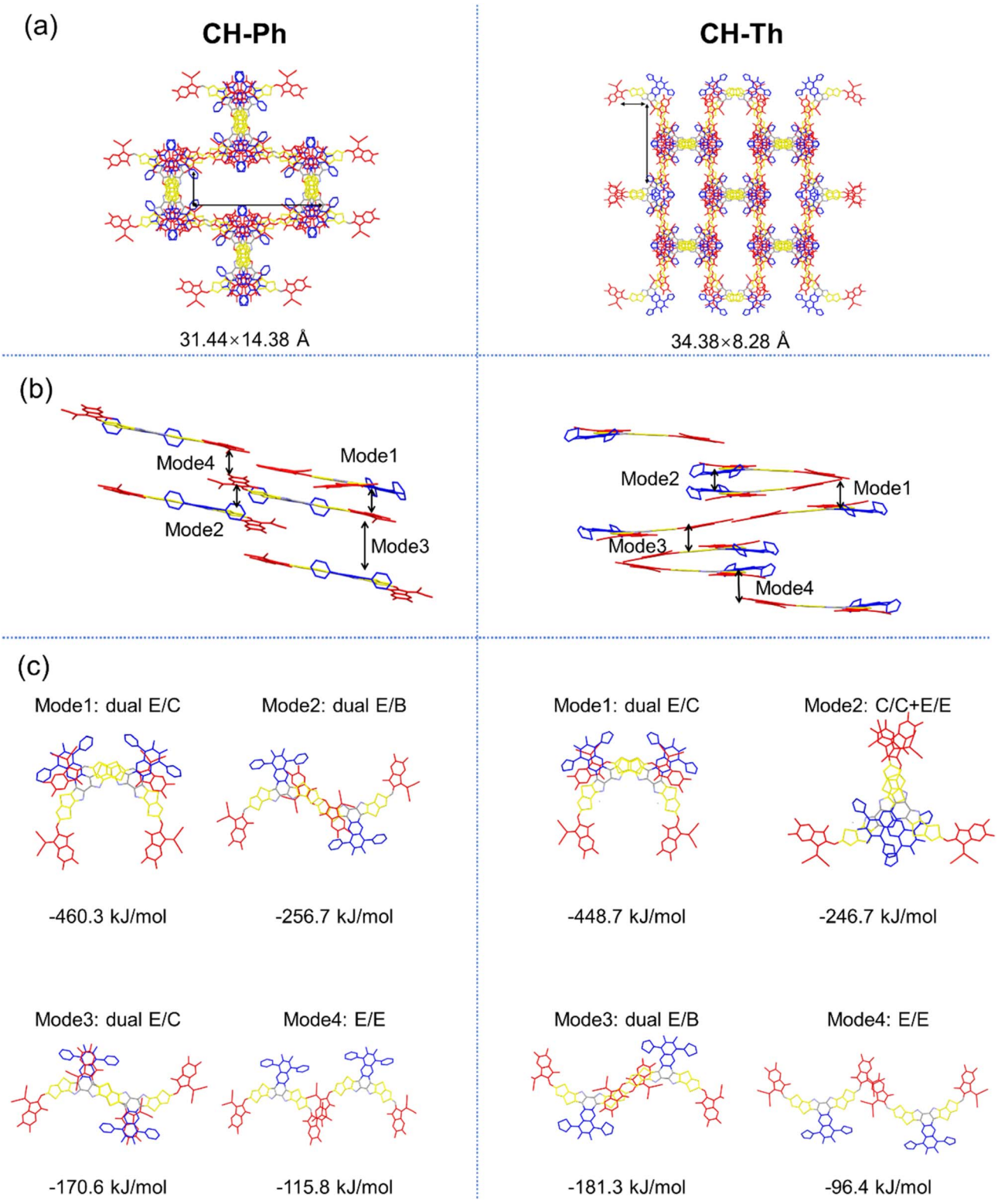

Fig. 3 (a) Topological structure of the 3D single-crystal packing from the top view. (b) The dominant intermolecular packing modes in NFAs. (c) Intermolecular potentials of the packing modes.

significantly improved J_{SC} and FF of the ternary devices enhanced the efficiency, which can be attributed to better light harvesting and superior charge separation and transport properties (Fig. S12). We have also fabricated devices with a non-chlorinated solvent *o*-xylene. Due to the relatively low solubility of CH-Th in *o*-xylene, the PCEs of CH-Th based binary and ternary devices (16.24% for PM6:CH-Th binary devices and 16.62% for PM6:CH6F:CH-Th ternary devices) were lower than

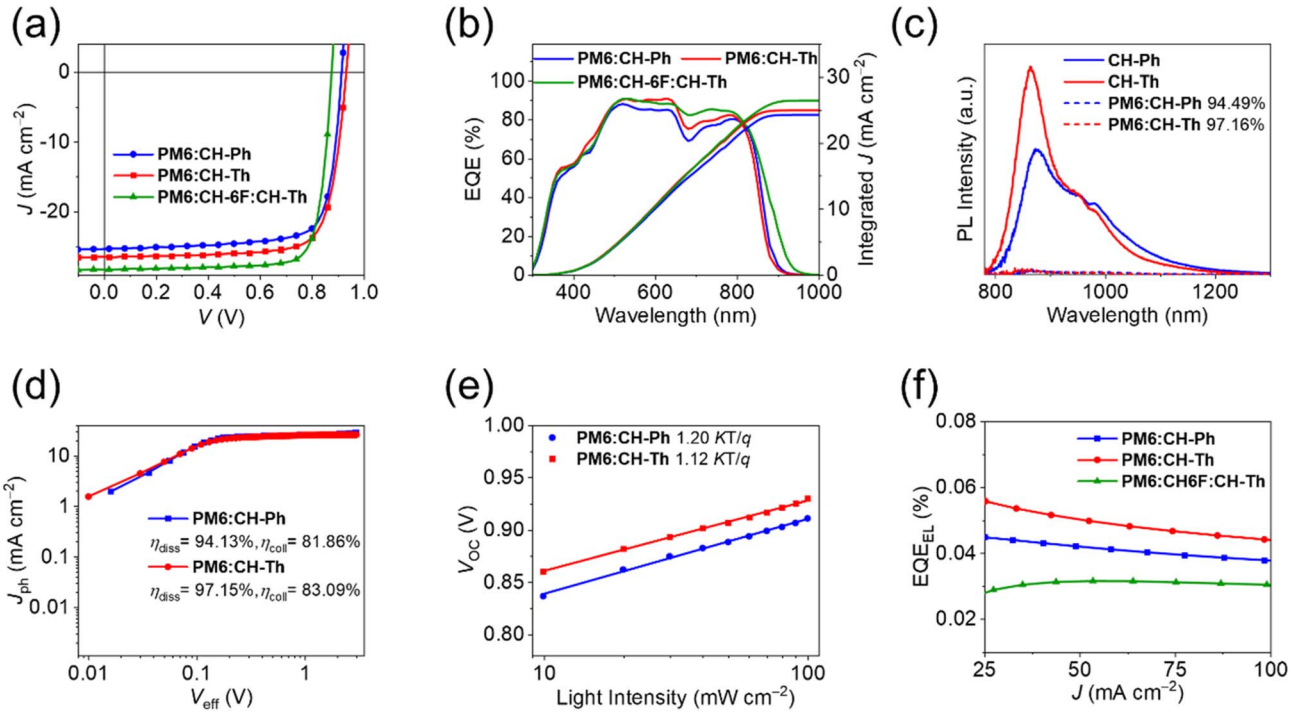

Fig. 4 (a) J–V characteristics of the optimal devices. (b) EQE spectra and integral J_{SC} values of the corresponding devices. (c) Photoluminescence (PL) spectra in neat and blend films showing PL quenching efficiency. (d) J_{ph} *versus* V_{eff} curves indicating η_{diss} and η_{coll}. (e) P_{light} dependence of V_{OC}. (f) The EQE_{EL} plots for optimized devices.

Table 1 Photovoltaic parameters for OSCs[a]

Active layer	V_{OC} [V]	J_{SC} [mA cm^{-2}]	J_{SC}^{EQE}[b] [mA cm^{-2}]	FF [%]	PCE [%]
PM6:CH-Ph	0.914 (0.910 ± 0.002)	25.30 (25.06 ± 0.38)	24.28	77.36 (76.60 ± 0.91)	17.89 (17.48 ± 0.30)
PM6:CH-Th	0.932 (0.927 ± 0.003)	26.41 (26.55 ± 0.14)	25.09	77.01 (75.84 ± 0.41)	18.96 (18.67 ± 0.09)
PM6:CH6F:CH-Th	0.876 (0.873 ± 0.002)	28.24 (28.13 ± 0.09)	26.86	80.62 (80.55 ± 0.16)	19.94 (19.79 ± 0.08)

[a] Average parameters with standard deviation obtained from 15 independent OSCs. [b] Current densities derived from integrating EQE plots.

those processed from chloroform. Comparatively, PM6:CH-Ph based devices maintained a PCE of 16.71%, which benefited from its good solubility both in *o*-xylene and chloroform (Tables S10–S12).

Photoluminescence (PL) measurements were performed to study charge transfer between the donor and acceptor. All binary blends exhibited strong PL quenching of acceptor emission. PM6:CH-Th showed the highest quenching efficiency (97.16%), followed by PM6:CH-Ph (94.49%) (Fig. 4c). This result indicates more efficient charge transfer within the PM6:CH-Th blend, which is consistent with its higher EQEs observed in the corresponding binary devices. Charge generation, transport, and recombination characteristics are further summarized in Fig. 4d and e. The exciton dissociation efficiency (η_{diss}) was 94.13% for PM6:CH-Ph and 97.15% for PM6:CH-Th. The charge collection efficiency (η_{coll}) reached 81.86% for PM6:CH-Ph and 83.09% for PM6:CH-Th. Trap-assisted recombination was analyzed using the exponential factor S in the relationship $V_{OC} \propto S \cdot \ln(P_{light})$. A value of S closer to kT/q indicates weaker trap-assisted recombination. The PM6:CH-Ph device gave the largest S (1.20 kT/q), followed by PM6:CH-Th (1.12 kT/q), confirming that trap-assisted recombination is suppressed in PM6:CH-Th-based devices. The energy loss of PM6:NFA-based devices was analyzed quantitatively to evaluate the impact of aromatic substituents on the phenazine core (Fig. S13). According to the detailed balance theory, the total energy loss (E_{loss}) can be partitioned into three parts: ΔE_1 is the Shockley–Queisser limit of V_{OC}, ΔE_2 is the radiative energy loss and ΔE_3 is the nonradiative energy loss. The overall E_{loss} for PM6:CH-Ph and PM6:CH-Th were 0.527 and 0.522 eV (Table S13). Particularly, the smaller nonradiative recombination energy loss value (ΔE_3) indicated by the larger EQE of electroluminescence (EQE_{EL}) of PM6:CH-Th can account for the overall smaller E_{loss} (Fig. 4f). The charge mobilities for the hole (μ_h) and electron (μ_e) were measured by the space-charge limited current (SCLC) method and are illustrated in Fig. S14 and S15. PM6:CH-Ph/PM6:CH-Th exhibited a hole mobility of 6.60/6.73 × 10^{-4} cm^2 V^{-1} s^{-1} and electron mobility of 5.75/5.92 × 10^{-4} cm^2 V^{-1} s^{-1}, respectively. The NFAs with substituted aromatic cores exhibited moderately high hole mobility and balanced hole-to-

electron mobility ratios. This is helpful to facilitate efficient charge extraction and suppress recombination. Notably, incorporating CH-Th into PM6:CH6F enhanced both hole and electron mobilities in the resulting ternary device with a more balanced charge mobility, which likely contributes to the highest observed FFs in these devices (Table S14). The PM6:CH-Ph and PM6:CH-Th based devices retained 90% of their initial efficiency after 230 h and 248 h, respectively after thermal aging at 65 °C (Fig. S16). Besides, the PM6:CH-Ph and PM6:CH-Th based devices retained 70% and 61% of their initial efficiency after 188 hours of light aging under the maximum power point (MPP) condition (Fig. S17).

The surfaces of PM6:CH-Ph, PM6:CH-Th and PM6:CH6F:CH-Th based blends were relatively smooth, with root-mean-square roughness (R_q) values of 0.82, 0.86 and 0.89 nm, respectively (Fig. 5a), which is sightly rougher than that of PM6:CH6F (0.79 nm, Fig. S18). To investigate how the substituted aromatic rings on the phenazine core affect phase separation, we performed AFM-based infrared (AFM-IR) spectroscopy to characterize the fibrillar network morphology and the nanoscale phase distribution of donor and acceptor materials in the blend films. The cyano group on the acceptor end-unit exhibits a distinct infrared absorption at 2216 cm^{-1}, which served as a spectroscopic label for acceptor mapping (Fig. 5b). In the corresponding AFM-IR images, donor and acceptor domains are colored blue and red, respectively. All binary blend films showed a typical co-continuous interpenetrating network.

To probe the molecular packing within blend films, GIWAXS measurements were performed and the corresponding data are summarized in Fig. 5c, S20 and Table S15. All blend films

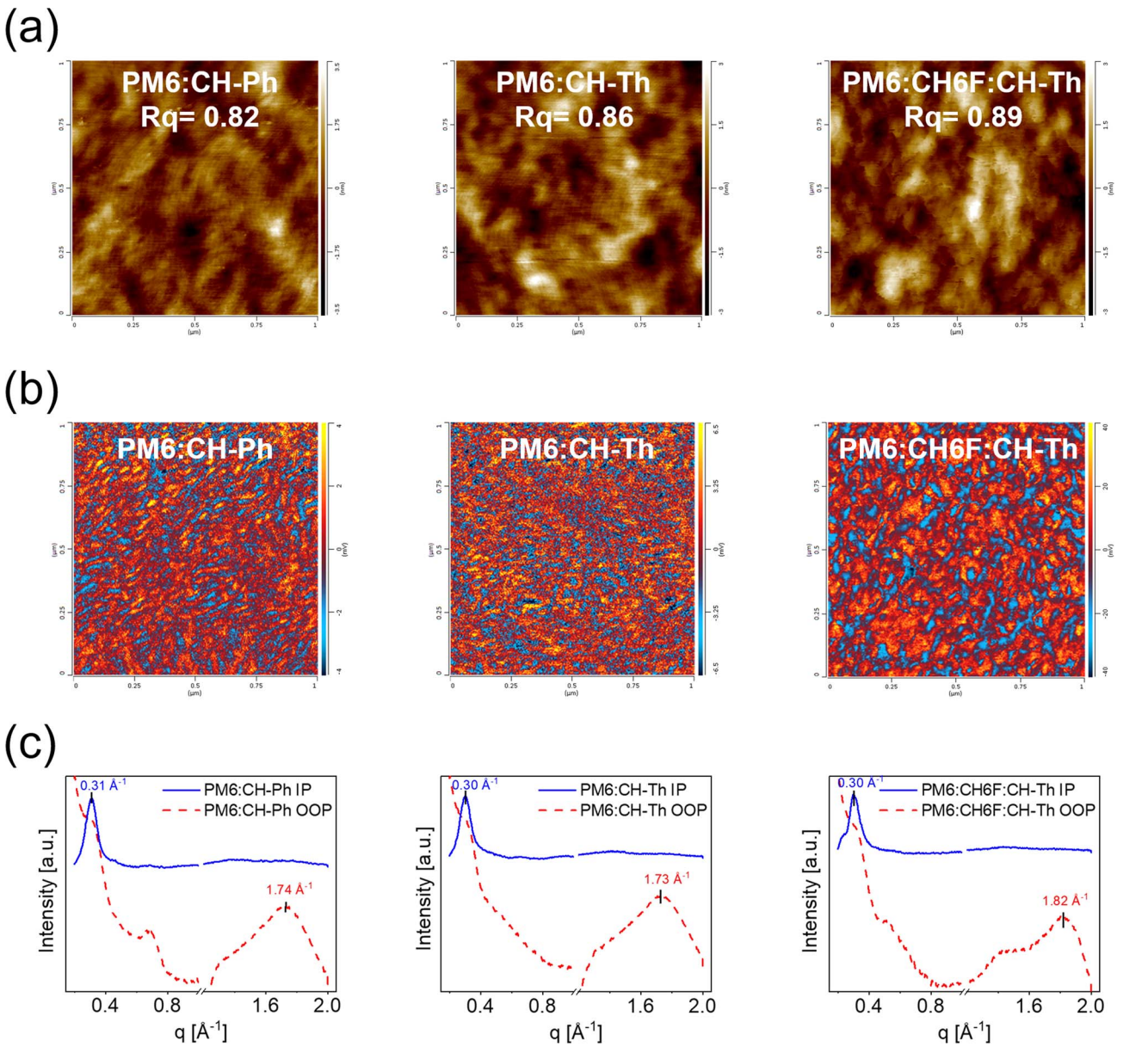

Fig. 5 (a) AFM phase images of blend films. (b) AFM-IR images of blend films. (c) OOP and IP line cuts derived from 2D-GIWAXS of blend films.

maintained a predominantly face-on molecular packing, evidenced by a strong (010) diffraction peak in the OOP direction. Owing to the substituted aromatic rings on the phenazine core, the π–π stacking distances for PM6:CH-Ph and PM6:CH-Th were 3.63 Å and 3.60 Å, respectively. The ternary blend PM6:CH6F:CH-Th showed a slightly smaller π–π distance of 3.46 Å. The CCLs along the OOP direction were 28.42, 32.90, and 41.39 Å for PM6:CH-Ph, PM6:CH-Th, and PM6:CH6F:CH-Th, respectively. Correspondingly, the CCLs along the IP direction were 94.55, 103.85, and 190.85 Å for the same blends, showing a consistently increasing trend that correlates well between both orientations. Such an enhanced long-range ordering in ternary devices is expected to facilitate charge transport and suppress recombination. Besides, during film formation, PM6:CH6F:CH-Th ternary films exhibited the smallest crystallization time of ∼2.0 s (Fig. S21), shorter than that of PM6:CH-Th (∼2.3 s) and PM6:CH-Ph (∼3.1 s). This indicates that CH-Th possesses strong crystallinity and can induce rapid crystallization of CH6F.

Conclusion

With the aim to enhance the intermolecular packing strength of NFAs, two new small molecule acceptors CH-Ph and CH-Th were designed and synthesized through employing different aromatic rings substituted on a specific position of the central phenazine core. Our research has revealed that the presence of different aromatic rings on the central core can cause a significant difference in molecular planarity, which in turn results in diverse packing and crystallinity in the active layer. To be specific, CH-Th, with its planar molecular structure resulting from noncovalent S–N secondary interactions, exhibited high crystallinity and achieved good morphology in the active layer. Consequently, the PM6:CH-Th-based binary cell achieved a good PCE of 18.96%. Given that CH-Th shows good miscibility with CH6F and can enhance its crystallinity, while CH6F itself exhibits a red-shifted absorption compared to CH-Th, the ternary OSCs of PM6:CH6F:CH-Th achieved a better PCE of 19.94% with a V_{OC} of 0.876 V, a J_{SC} of 28.24 mA cm^{-2}, and an FF of 80.62%. Our work demonstrates an effective strategy for tuning crystallinity through central-core aromatic substitution, offering a practical method to guide the molecular design of high-performance NFAs.

Author contributions

The synthesis work was carried out by Ruibin Bian; the device optimization and measurements were carried out by Xiangjian Cao. Ruibin Bian, Wenkai Zhao and Guankui Long performed the DFT calculations. Yongsheng Chen and Zhaoyang Yao conceived and directed the study, and revised the manuscript. Shuhui Ding, Chenxi Li and Xiangjian Wan helped with the analysis of the data and commented on the manuscript.

Conflicts of interest

The authors declare no competing interests.

Data availability

The data that support the findings of this study are available from the corresponding author upon reasonable request.

CCDC 2518501 and 2417397 contain the supplementary crystallographic data for this paper.[72a,b]

Supplementary information (SI): the materials and methods, instruments, detailed synthesis procedures, DFT calculations and all the relevant data. See DOI: https://doi.org/10.1039/d5ta10460b.

Acknowledgements

The authors gratefully acknowledge the financial support from the Ministry of Science and Technology of the People's Republic of China (National Key R&D Program of China, 2022YFB4200400), National Natural Science Foundation of China (22479081, 22309090, 52025033, 22361132530, 52373189), Natural Science Foundation of Tianjin (23JCZDJC01160) and Haihe Laboratory of Sustainable Chemical Transformations.

References

1 Z. Xiao, S. Li, J. Liu, X. Chen, Z. Suo, C. Li, X. Wan and Y. Chen, *Sol. RRL*, 2024, **8**(11), 2400206.
2 Q. R. Ye, W. Song, Y. Q. Bai, Z. Y. Chen, P. F. Ding, J. F. Ge, Y. Y. Meng, B. Han, X. Zhou and Z. Y. Ge, *Energy Environ. Sci.*, 2025, **18**(9), 4373–4383.
3 Z. Wei, Y. Wang, Y. Li, S. Gong, X. Jiang, Y. Liu, D. Zhang, Y. Cho, A. Zhang, L. Gao, *et al.*, *Joule*, 2025, **9**(7), 101996.
4 S. Zeng, H. Li, S. Liu, T. Xue, K. Zhang, L. Hu, Z. Cai, Y. Cui, H. Wang, M. Zhang, *et al.*, *Energy Environ. Sci.*, 2025, **18**(5), 2318–2329.
5 X. Zheng, L. Zuo, F. Zhao, Y. Li, T. Chen, S. Shan, K. Yan, Y. Pan, B. Xu, C.-Z. Li, *et al.*, *Adv. Mater.*, 2022, **34**(17), 2200044.
6 N. Yang, S. Q. Zhang, Y. Cui, J. Q. Wang, S. H. Cheng and J. H. Hou, *Nat. Rev. Mater.*, 2025, **10**(6), 404–424.
7 R. Zeng, M. Zhang, X. Wang, L. Zhu, B. Hao, W. Zhong, G. Zhou, J. Deng, S. Tan, J. Zhuang, *et al.*, *Nat. Energy*, 2024, **9**(9), 1117–1128.
8 W. Wei, X. Yuan, X. Zhou, Y. Li, S. Lee, J. Xu, Y. Zhang, H. Feng, Q. Jiang, J. Wu, *et al.*, *Angew. Chem., Int. Ed.*, 2025, **64**(48), e202517485.
9 Y. Shi, J. Wang, X. Song, S. Wei, T. Yuan, Y. Li, X. Li, Y. Zhang, L. Fan and J. Hou, *Joule*, 2025, **9**(8), 102013.
10 M. Yang, Y. Wang, X. Han, B. Yin, X. Zhou, Z. Chen, J. Zhong, Y. Li, W. Wei, Z. Liu, *et al.*, *Sci. China:Chem.*, 2025, **69**(1), 283–292.
11 J. M. Huang, Z. Lu, J. Q. He, H. Hu, Q. Liang, K. Liu, Z. W. Ren, Y. K. Zhang, H. Y. Yu, Z. J. Zheng, *et al.*, *Energy Environ. Sci.*, 2023, **16**(3), 1251–1263.
12 Y. Z. Huang, C. Z. Jiang, Y. Zhu, S. C. Zhang, G. H. Li, Z. Y. Yao, C. X. Li, X. J. Wan and Y. S. Chen, *Org. Electron.*, 2022, **110**, 106642.

13 Y. Zhao, Z. Li, C. Deger, M. Wang, M. Peric, Y. Yin, D. Meng, W. Yang, X. Wang, Q. Xing, *et al.*, *Nat. Sustain.*, 2023, **6**(5), 539–548.
14 S. Dong, T. Jia, K. Zhang, J. Jing and F. Huang, *Joule*, 2020, **4**(9), 2004–2016.
15 C. Han, Z. Jin, C. Shen, M. Liu, W. Song, Q. Liu and Z. Ge, *Adv. Energy Mater.*, 2025, **15**(31), 2501682.
16 Z. You, J. Wen, W. Liu, Z. Fink, X. Wu, H.-G. Seong, Y. Wang, L. Zhang, X. Wang, T. P. Russell, *et al.*, *Adv. Mater.*, 2025, **37**(15), 2500450.
17 J. Liu, Z. Suo, L. Li, W. Zhao, J. Huo, J. Chen, G. Long, Z. Yao, C. Li, X. Wan, *et al.*, *Energy Environ. Sci.*, 2025, **18**(18), 8658–8666.
18 J. Yi, G. Zhang, H. Yu and H. Yan, *Nat. Rev. Mater.*, 2024, **9**(1), 46–62.
19 R. Sun, T. Wang, X. Yang, Y. Wu, Y. Wang, Q. Wu, M. Zhang, C. J. Brabec, Y. Li and J. Min, *Nat. Energy*, 2022, **7**(11), 1087–1099.
20 Y. Shen, Y. Wang, Y. Zhang, C. Wang, Y. Zhu, Y. Kong, A. Wupur, C. Zhang, M. Wang, C. Gao, *et al.*, *Sol. RRL*, 2025, **9**(21), e202500614.
21 P. Wang, X. Cao, W. Zhao, Y. Zhang, Z. Xu, Z. Zhang, G. Li, G. Long, X. Wan, C. Li, *et al.*, *Adv. Funct. Mater.*, 2026, **36**(14), e18113.
22 Y. Huo, B. Cheng, L. Kan, X. Guo, X. Xia, C. Han, S. Ning, W. Hou, F. Liu and M. Zhang, *Adv. Funct. Mater.*, 2026, **36**(14), e14342.
23 X. Liao, Z. Li, S. Lai, H. Ding, J. Yu, Y. Fu, P. Zhu, X. Lu, H. Zhu and Y. Chen, *Energy Environ. Sci.*, 2025, **18**(20), 9125–9137.
24 J. Zhang, W. Wei, Z. Luo, Z. Chen, R. Ma, M. Wang, Y. Luo, Y. Chan, Z. Bi, Y. Li, *et al.*, *Angew. Chem., Int. Ed.*, 2025, **64**, e202512237.
25 L. Zhang, Z. Zhuo, X. Ma, H. Tian, X. Zhao, Y. Xie, K. Yang, B. H. Lee, X. Zhu, H. Y. Woo, *et al.*, *Energy Environ. Sci.*, 2025, **18**(20), 9171–9182.
26 Y. Yang, L. Wei, L. Zhan, Y. Liu, H. Lu, X. Wu, A. Wupur, T. Chen, J. Yu, X. Sun, *et al.*, *Adv. Mater.*, 2025, **37**(44), e10980.
27 R. Zeng, F. Han, W. Zhong, M. Zhang, S. Tan, Y. Lin, J. Deng, G. Zhou, L. Kan, L. Zhu, *et al.*, *Adv. Mater.*, 2025, **37**(28), 2501812.
28 R. Ma, Z. Luo, Y. Zhang, L. Zhan, T. Jia, P. Cheng, C. Yan, Q. Fan, S. Liu, L. Ye, *et al.*, *Sci. China Mater.*, 2025, **68**(6), 1689–1701.
29 W. Ni, X. Wan, M. Li, Y. Wang and Y. Chen, *Chem. Commun.*, 2015, **51**(24), 4936–4950.
30 Y. Lin, J. Wang, Z.-G. Zhang, H. Bai, Y. Li, D. Zhu and X. Zhan, *Adv. Mater.*, 2015, **27**(7), 1170–1174.
31 Y. Yang, Z.-G. Zhang, H. Bin, S. Chen, L. Gao, L. Xue, C. Yang and Y. Li, *J. Am. Chem. Soc.*, 2016, **138**(45), 15011–15018.
32 W. Zhao, S. Li, H. Yao, S. Zhang, Y. Zhang, B. Yang and J. Hou, *J. Am. Chem. Soc.*, 2017, **139**(21), 7148–7151.
33 H. Zhang, H. Yao, J. Hou, J. Zhu, J. Zhang, W. Li, R. Yu, B. Gao, S. Zhang and J. Hou, *Adv. Mater.*, 2018, **30**(28), 1800613.
34 W. Zhu, A. P. Spencer, S. Mukherjee, J. M. Alzola, V. K. Sangwan, S. H. Amsterdam, S. M. Swick, L. O. Jones, M. C. Heiber, A. A. Herzing, *et al.*, *J. Am. Chem. Soc.*, 2020, **142**(34), 14532–14547.
35 D. Mo, H. Chen, J. Zhou, N. Tang, L. Han, Y. Zhu, P. Chao, H. Lai, Z. Xie and F. He, *J. Mater. Chem. A*, 2020, **8**(18), 8903–8912.
36 C. Li, J. Zhou, J. Song, J. Xu, H. Zhang, X. Zhang, J. Guo, L. Zhu, D. Wei, G. Han, *et al.*, *Nat. Energy*, 2021, **6**(6), 605–613.
37 X. Gu, R. Zeng, Y. Hou, N. Yu, J. Qiao, H. Li, Y. Wei, T. He, J. Zhu, J. Deng, *et al.*, *Angew. Chem., Int. Ed.*, 2024, **63**(34), e202407355.
38 J. Xu, F. Lin, L. Zhu, M. Zhang, T. Hao, G. Zhou, K. Gao, Y. Zou, G. Wei, Y. Yi, *et al.*, *Adv. Energy Mater.*, 2022, **12**(34), 2201338.
39 H. Lai and F. He, *Adv. Energy Mater.*, 2020, **10**(47), 2002678.
40 X. Wang, H. Lu, Y. Liu, A. Zhang, N. Yu, H. Wang, S. Li, Y. Zhou, X. Xu, Z. Tang, *et al.*, *Adv. Energy Mater.*, 2021, **11**(45), 2102591.
41 X. Bi, X. Cao, T. He, H. Liang, Z. Yao, J. Yang, Y. Guo, G. Long, B. Kan, C. Li, *et al.*, *Small*, 2024, **20**(32), 2401054.
42 J. Guo, X. Cao, Z. Xu, T. He, X. Bi, Z. Yao, Y. Guo, G. Long, C. Li, X. Wan, *et al.*, *J. Mater. Chem. A*, 2025, **13**(1), 356–367.
43 Z. Xu, X. Cao, Z. Yao, W. Zhao, W. Shi, X. Bi, Y. Li, Y. Guo, G. Li, G. Long, *et al.*, *Angew. Chem., Int. Ed.*, 2025, **64**(22), e202421289.
44 Y. Shi, Y. Chang, K. Lu, Z. Chen, J. Zhang, Y. Yan, D. Qiu, Y. Liu, M. A. Adil, W. Ma, *et al.*, *Nat. Commun.*, 2022, **13**(1), 3256.
45 J. Zhang, R. Ma, R. Li, J. Tang, D. Luo, L. Chen, Z. Chen, Y. Wang, H. Chen, J. Feng, *et al.*, *Nat. Commun.*, 2025, **16**(1), 11480.
46 X. Li, X. Kong, G. Sun and Y. Li, *eScience*, 2023, **3**(5), 100171.
47 Y. Zou, H. Chen, X. Bi, X. Xu, H. Wang, M. Lin, Z. Ma, M. Zhang, C. Li, X. Wan, *et al.*, *Energy Environ. Sci.*, 2022, **15**(8), 3519–3533.
48 X. J. Cao, P. R. Wang, X. Y. Jia, W. K. Zhao, H. B. Chen, Z. Xiao, J. Q. Li, X. Q. Bi, Z. Y. Yao, Y. X. Guo, *et al.*, *Angew. Chem., Int. Ed.*, 2025, **64**(5), e202417244.
49 Y. Chen, H. Chen, Y. Zou, C. Li, X. Wan and C. Yao, Organic photoelectric compound and preparation method and application thereof, CN116514835A, 2023.
50 X. Zhu, W. Liu, S. Xu and Z. Zhou, Quinoxaline derivative acceptor material, and preparation method and applications thereof, CN110283185A, 2019.
51 L.-K. Ma, Y. Chen, P. C. Y. Chow, G. Zhang, J. Huang, C. Ma, J. Zhang, H. Yin, A. M. Hong Cheung, K. S. Wong, *et al.*, *Joule*, 2020, **4**(7), 1486–1500.
52 Y. Cheng, J. Xu, S. Liang, M. Li, B. Wang, H. Fang, Q. Tan, H. Wang, Z. Lu, C. Xiao, *et al.*, *ACS Appl. Mater. Interfaces*, 2025, **17**(32), 45990–45998.
53 S. Oh, K. Bae, D. Jeong, T. N.-L. Phan, J.-W. Lee and B. J. Kim, *Adv. Funct. Mater.*, 2025, **35**(39), 2502707.
54 C. Gaoda, C. Yuan, P. Zhengxing, J. Yanyan, Z. Xinhui, Y. Dian, Y. Han, C. Yuzhong, C. Y. C. Philip, W. Kam Sing, *et al.*, *Nano Energy*, 2020, **76**, 105087.

55 X. Wang, X. Shen, J. Wang, F. Bi, H. Jiang, H. Lu, C. Sun, C. Yang, Y. Li and X. Bao, *Energy Environ. Sci.*, 2025, **18**(11), 5586–5598.
56 J. Wang, C. Sun, Y. Li, F. Bi, H. Jiang, C. Yang, X. Bao and J. Chu, *Nat. Commun.*, 2025, **16**(1), 1784.
57 C. Sun, J. Wang, F. Bi, H. Jiang, C. Yang, Y. Li, J. Chu and X. Bao, *Energy Environ. Sci.*, 2025, **18**(2), 862–873.
58 A. D. Becke, *J. Chem. Phys.*, 1993, **98**(7), 5648–5652.
59 P. C. Hariharan and J. A. Pople, *Mol. Phys.*, 1974, **27**(1), 209–214.
60 W. Yan, Q. Zhang, Q. Qin, S. Ye, Y. Lin, Z. Liu, Z. Bian, Y. Chen and C. Huang, *Dyes Pigm.*, 2015, **121**, 99–108.
61 H. Chen, Z. Zhang, P. Wang, Y. Zhang, K. Ma, Y. Lin, T. Duan, T. He, Z. Ma, G. Long, *et al.*, *Energy Environ. Sci.*, 2023, **16**(4), 1773–1782.
62 P. Li, W. Xiong, J. Wang, J. Hao, M. Li, B. Wang, Y. Chen, W. Si, H. Ren, G. Li, *et al.*, *Adv. Mater.*, 2023, **35**(28), 2301876.
63 G. He, Z. Li, X. Wan, Y. Liu, J. Zhou, G. Long, M. Zhang and Y. Chen, *J. Mater. Chem.*, 2012, **22**(18), 9173–9180.
64 K. Liu, Y. Jiang, F. Liu, G. Ran, M. Wang, W. Wang, W. Zhang, Z. Wei, J. Hou and X. Zhu, *Adv. Mater.*, 2025, **37**(7), 2413376.
65 D. Qiu, L. Zhang, H. Zhang, A. Tang, J. Zhang, Z. Wei and K. Lu, *J. Mater. Chem. A*, 2025, **13**(6), 4237–4246.
66 H. Chen, X. Cao, P. Wang, F. Huang, Y. Zhang, H. Liang, X. Bi, T. He, W. Feng, Y. Guo, *et al.*, *J. Mater. Chem. A*, 2023, **11**(46), 25368–25376.
67 H. Hu, M. Ghasemi, Z. Peng, J. Zhang, J. J. Rech, W. You, H. Yan and H. Ade, *Adv. Mater.*, 2020, **32**(49), 2005348.
68 P. W. M. Blom, M. J. M. de Jong and J. J. M. Vleggaar, *Appl. Phys. Lett.*, 1996, **68**(23), 3308–3310.
69 W. Gao, F. Qi, Z. Peng, F. R. Lin, K. Jiang, C. Zhong, W. Kaminsky, Z. Guan, C.-S. Lee, T. J. Marks, *et al.*, *Adv. Mater.*, 2022, **34**(32), 2202089.
70 L. Wang, Q. An, L. Yan, H.-R. Bai, M. Jiang, A. Mahmood, C. Yang, H. Zhi and J.-L. Wang, *Energy Environ. Sci.*, 2022, **15**(1), 320–333.
71 M. Zhang, X. Guo, W. Ma, H. Ade and J. Hou, *Adv. Mater.*, 2015, **27**(31), 4655–4660.
72 (*a*) CCDC 2518501: Experimental Crystal Structure Determination, 2026, DOI: 10.5517/ccdc.csd.cc2qjpzy; (*b*) CCDC 2417397: Experimental Crystal Structure Determination, 2026, DOI: 10.5517/ccdc.csd.cc2m4hkv.